

# 1 A Self-Assembled Graphene Ribbon Device on SiC

2 Bi-Yi Wu, Yanfei Yang, Albert F. Rigosi, Jiuning Hu, Hsin-Yen Lee, Guangjun Cheng, Vishal Panchal,  
3 Mattias Kruskopf, Hanbyul Jin, Kenji Watanabe, Takashi Taniguchi, David B. Newell,  
4 Randolph E. Elmquist,\* and Chi-Te Liang\*



Cite This: <https://dx.doi.org/10.1021/acsaelm.9b00696>



Read Online

ACCESS |



Metrics & More



Article Recommendations

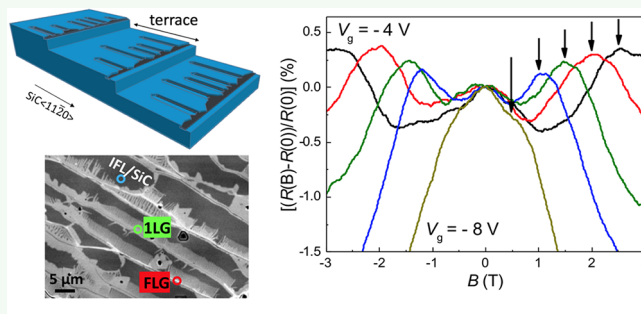


Supporting Information

5 **ABSTRACT:** Graphene ribbons, which may be fabricated by a  
6 wide variety of experimental techniques such as chemical  
7 processing, unzipping or etching of carbon nanotubes, molecular  
8 precursors, ion implantation, and so on, can find promising  
9 applications in interconnects, terahertz sensors, and plasmonic  
10 devices. Here we report measurements on self-assembled graphene  
11 ribbons that are prepared by a controlled high-temperature  
12 sublimation technique. The epitaxial graphene ribbons on SiC  
13 can be readily and efficiently located by confocal laser scanning  
14 microscopy for device fabrication using a removable metal  
15 protection layer to avoid contamination of the graphene and  
16 hexagonal boron nitride to serve as a top-gate dielectric spacer.

17 These self-assembled graphene ribbons have smooth edges, and the observation of a magnetoresistance side peak in such a structure  
18 is consistent with diffusive boundary scattering in the quasi-ballistic regime. In contrast, graphene ribbons defined by electron-beam  
19 lithography and subsequent conventional reactive ion etching on the same SiC wafer only show pronounced negative  
20 magnetoresistance due to strong disorder in the edge structures (chemical dopants, the resolution of electron-beam lithography,  
21 etc.). Our experimental approaches are applicable to wafer-scale, graphene-based integrated circuits.

22 **KEYWORDS:** *graphene, ribbon, self-assembled, sublimation, contamination-free, magnetotransport*



## 23 ■ INTRODUCTION

24 Graphene, which is a single layer of carbon atoms arranged in a  
25 honeycomb lattice, continues to attract a great deal of  
26 worldwide interest because of its extraordinary physical  
27 properties. Graphene is an ideal two-dimensional (2D) system  
28 for one to probe fascinating physical phenomena such as the  
29 unconventional integer quantum Hall effect,<sup>1,2</sup> the fractional  
30 quantum Hall effect,<sup>3,4</sup> Klein tunneling,<sup>5</sup> and so on. By  
31 imposing additional confinement upon a graphene 2D system,  
32 one can create narrow ribbon devices from graphene. In  
33 graphene-based microstructures and nanostructures, edge  
34 effects and boundary scattering strongly affect the electrical  
35 properties of devices.<sup>6</sup> For example, irregular edges can cause  
36 unwanted quantum dot structures in graphene nanoribbons,  
37 giving rise to the Coulomb blockade effect.<sup>7,8</sup> Moreover,  
38 backscattering from irregular graphene edges can significantly  
39 reduce the mobility with decreasing device width.<sup>9</sup> Therefore,  
40 atomically smooth edges are highly desirable for graphene-  
41 based mesoscopic devices. In most cases, micrometer- or  
42 nanometer-sized graphene devices are fabricated by electron-  
43 beam (e-beam) lithography when PMMA is often used as the  
44 e-beam resist. It is known that graphene could be doped by  
45 PMMA and its residues, which are difficult to be fully removed  
46 after e-beam lithography and subsequent processes. The

presence of PMMA and other organic residues may 47  
significantly degrade the quality of bulk graphene and the 48  
smoothness of graphene edges and introduce carrier density 49  
inhomogeneity, resulting in unintentional variable range 50  
hopping (VRH) transport in graphene-based devices.<sup>10,11</sup> 51

Here we report self-assembled epitaxial graphene ribbons on 52  
SiC prepared by a controlled high-temperature sublimation 53  
technique, similar to the approach of growing large-area 54  
monolayer graphene on SiC.<sup>12</sup> In our work, graphene ribbons, 55  
whose widths are a couple of hundred nanometers, can be 56  
readily and efficiently located (10 min over an area of 360 μm 57  
× 360 μm) by confocal laser scanning microscopy (CLSM).<sup>13</sup> 58  
During our fabrication process, the graphene ribbon and its 59  
edges were completely protected by a 20 nm thick Au layer to 60  
avoid contamination of PMMA residues, leading to clean 61  
graphene surface and smooth graphene ribbon edges. We 62  
observed an anomalous magnetoresistance (MR) peak 63  
corresponding to the magnetic commensurability effect 64

Received: October 20, 2019

Accepted: January 2, 2020

Published: January 2, 2020

65 between cyclotron radius and the ribbon width.<sup>14–16</sup> We also  
66 studied the evolution of the MR peak with varying the top gate  
67 voltage applied across a thin hexagonal boron nitride (h-BN)  
68 dielectric. In contrast, on the same SiC substrate, a graphene  
69 ribbon etched by reactive ion etching (RIE) only shows large  
70 negative MR and no MR side peak is observed, which indicates  
71 that the edge smoothness is substantially lower than that of the  
72 self-assembled graphene ribbon. Our high-quality, self-  
73 assembled graphene ribbons may find promising applications  
74 in interconnects,<sup>17,18</sup> plasmonic devices,<sup>19,20</sup> energy storage,<sup>21</sup>  
75 and terahertz sensors.<sup>22,23</sup> Our characterization approach based  
76 on efficient CLSM studies of high-quality self-assembled  
77 graphene ribbons is portable to other 2D materials.

78 Before describing our experimental results, we would like to  
79 mention the work on graphene nanoribbons grown on SiC. It  
80 is possible to grow self-organized graphene nanoribbons (as  
81 narrow as 40 nm) as specified positions on a templated SiC  
82 substrate.<sup>24</sup> This approach allows researchers to fabricate  
83 10000 top-gated graphene transistors on a 0.24 cm<sup>2</sup> SiC chip.<sup>24</sup>  
84 Room-temperature ballistic transport in epitaxially grown  
85 graphene nanoribbons on SiC on a length scale longer than  
86 10 μm can be observed.<sup>25</sup> It is also possible to observe electron  
87 interference<sup>26</sup> in graphene nanoribbons grown on side-walls of  
88 SiC mesa structures.<sup>27</sup> Recently, nanoscale imaging of electric  
89 pathways in epitaxial graphene nanoribbons has been  
90 reported.<sup>28</sup>

91 **Fabrication.** In our work, graphene ribbons are grown  
92 epitaxially on SiC in ≈103 kPa ultrahigh-purity Ar gas at  
93 ≈1900 °C within ≈200 s with heating and cooling rates both  
94 ≈1 °C/s. The SiC substrate is positioned with the Si-  
95 terminated surface placed directly against a glassy graphite  
96 disk,<sup>29</sup> as shown in Figure 1a. In this case, the gas diffusion is  
97 limited by the small space between SiC and graphite, and the  
98 partial pressure of various decomposition byproducts at the  
99 surface of SiC approaches equilibrium. This environment  
100 stabilizes the Si loss rate and helps to ensure uniform growth at  
101 temperatures around ≈1900 °C.<sup>30</sup> At such a high temperature,  
102 the SiC surface morphology reconstructs to form broad  
103 terraces (Figure 1b). Meanwhile, primarily Si as well as other  
104 species such as silicon dicarbide and disilicon carbide are  
105 produced by sublimation. Decomposition of SiC occurs  
106 preferably along the terrace edge, as shown in Figure 1c,  
107 making regular indentations on the edge. As Si species leave  
108 the surface, carbon atoms accumulate on the SiC surface and  
109 recombine to form continuous graphene or graphene ribbons  
110 (Figure 1d). Since the diffusion of C atoms on SiC surface is  
111 anisotropic,<sup>31</sup> graphene ribbons are more attainable for wide  
112 and parallel terrace morphology, as shown in Figures 1d–f. In  
113 our study, large-area and continuous graphene is usually  
114 produced on SiC surface with narrow terraces.<sup>29,32</sup> We note  
115 that large-area monolayer graphene can be grown on  
116 ultrashallow SiC terraces by using polymer-assisted sublima-  
117 tion growth (PASG).<sup>33</sup> Figure 1g shows that the thickness of  
118 the sublimation area is ≈0.26 nm (Supporting Information  
119 S1), indicating decomposition of a single atomic layer of  
120 SiC(0001).<sup>34,35</sup> In this work, we produced arrays of graphene  
121 ribbons with width of a couple of hundred nanometers (Figure  
122 2a). The edges in natural graphene ribbon arrays form  
123 primarily along the SiC <1120> direction (Supporting  
124 Information S2). The edge configuration is therefore mainly  
125 armchair. It may be possible to grow zigzag edge ribbons by  
126 lithographically patterned trenches in SiC.<sup>36</sup>

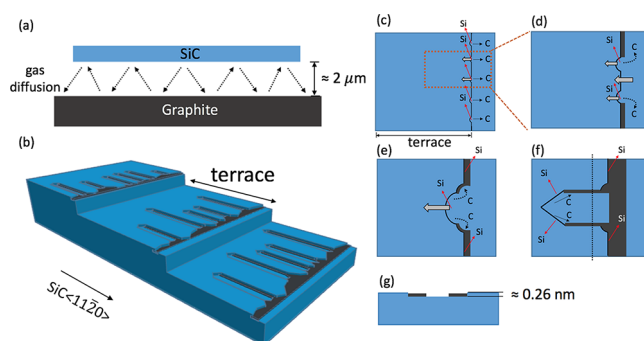


**Figure 1.** Schematic diagrams showing the growth mechanism of self-assembled graphene ribbons on SiC. The blue regions correspond to SiC/buffer layer, and the dark gray regions correspond to graphene ribbons or large-area graphene. (a) Schematic diagram showing the setup during the growth process. A SiC substrate is placed on a graphite. The distance between SiC and the glassy graphite surface is ≈2 μm, limited only by surface flatness, and this space confines the gas diffusion (dashed arrows). (b) Graphene ribbons grown from the edges of terraces. (c) Top view of the growth processes of graphene ribbons. Si atoms sublimate preferentially (as indicated by red arrows) from equally spaced positions on the edge of terraces, forming indentations. (d–f) A magnification of the selected area shown in (c). (d) Carbon atoms rearrange to form graphene ribbons along the edge of the terrace. The SiC decomposition rate at the center of a pair of indentations becomes faster. (e) Direction of Si loss is determined by the geometric limitation caused by preferred crystal orientation<sup>36</sup> and becomes straight to the left as indicated by the gray arrow. (f) Carbon atoms further rearrange to form long graphene ribbons along the edge. On the right, large-area monolayer graphene can be grown along the edge of the terrace. (g) Side view of the SiC substrate along the dashed line in shown in (f). The decomposition of SiC(0001) is layer by layer, with each basal plane of thickness ≈0.26 nm.

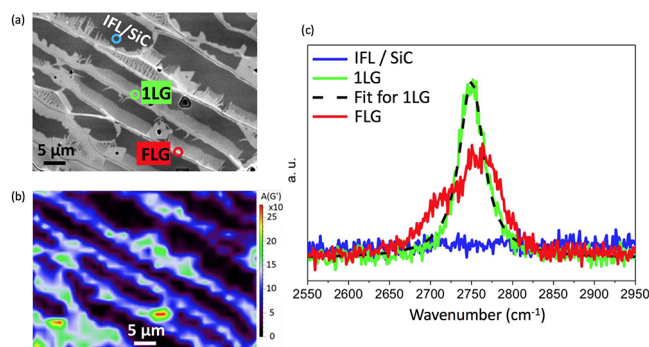


**Figure 2.** (a) Large-area CLSM image taken on a grown sample. As will be shown later, the blue, green, and red circles indicate the IFL/SiC, monolayer graphene, and multilayer graphene, respectively. (b) Map of the integrated G'(2D) peak from Raman spectra in the same region as indicated in (a). (c) Raman spectra of the blue, green, and red circles which are indicated in (a). The Raman spectra show the regions around the G'(2D) band, with IFL/SiC (the blue curve), monolayer graphene (the green curve), and multilayer graphene (the red curve), and the fit to a Lorentzian for 1LG (the dashed curve in black).

Our novel fabrication process adopts CLSM images to select individual, well-formed graphene ribbons and nearby alignment marks for e-beam lithography. Previously, scanning electron microscope (SEM) or atomic force microscope (AFM) imaging of selected graphene regions were usually required for device fabrication by e-beam lithography due to their high resolution. However, graphene may be doped by the

134 high-energy electron beams emitted by an SEM or damaged by  
 135 an AFM tip. It has been demonstrated that CLSM is a  
 136 noninvasive method to evaluate the thickness of graphene on  
 137 SiO<sub>2</sub> and SiC substrates.<sup>13</sup> The brightness contrast of a CLSM  
 138 intensity image depends on the reflected energy from different  
 139 materials. In the case of graphene, the reflected intensity is  
 140 sensitive to the number of layers. The high spatial resolution of  
 141 CLSM ( $\sim 150$  nm) is sufficient to identify the graphene  
 142 ribbons with widths of a couple of hundred nanometers. Figure  
 143 2a shows a CLSM intensity image of graphene ribbons on SiC.  
 144 Figure 2b shows a Raman map of integrated G'(2D) peak of  
 145 the same region. Figure 2c shows that the Raman spectra taken  
 146 on the blue, green, and red circles which are indicated in  
 147 Figure 2a. The absence of the G'(2D) peak in the blue curve  
 148 indicates that the darker regions correspond to the interfacial  
 149 layer (IFL) or bare SiC which are both electrically insulating.  
 150 The green curve shows a symmetric G'(2D) peak centered at  
 151 around 2750 cm<sup>-1</sup> which can be well fitted by a single  
 152 Lorentzian, as shown in the dashed curve in black in Figure 2c.  
 153 Therefore, these regions (labeled by the green circle)  
 154 correspond to monolayer graphene (1LG). The wide and  
 155 asymmetric G'(2D) peak in the red Raman spectra indicates  
 156 that the region within the red circle is multilayer graphene. We  
 157 note that similar monolayer graphene ribbons (1LG) have  
 158 been probed by Raman studies.<sup>13</sup> No increase in the D-peak  
 159 band (centered at around 1400 cm<sup>-1</sup>) for single-layer graphene  
 160 ribbons and two-layer graphene can be seen. There is little  
 161 change of the Raman D-band from the bare SiC background.<sup>13</sup>

162 We used a contamination-free method<sup>37</sup> to fabricate  
 163 graphene ribbon devices. To this end, we began fabrication  
 164 by evaporating a 20 nm thick Au layer,<sup>37</sup> which protected the  
 165 graphene ribbon from PMMA residues used in the subsequent  
 166 lithography (Figure 3a,b). The selected ribbon and areas for  
 167 electrical contacts were covered with a thicker Au pattern<sup>37</sup>  
 168 which served as a mask (Figure 3c) when the adjacent area of  
 169 graphene was removed by Ar plasma RIE. Then, we deposited  
 170 Pt contacts to the graphene ribbon ends and etched the Au  
 171 layer on top of graphene ribbon by dilute aqua regia (Figure  
 172 3d). We can completely remove the Au protection layer from  
 173 the EG region by immersing the devices in dilute aqua regia  
 174 (by volume, HNO<sub>3</sub>:HCl:H<sub>2</sub>O = 1:3:4) for 45 s at room  
 175 temperature (the solution usually self-heats to 30 °C)<sup>38</sup>  
 176 (Figure 3d). This fabrication process initiates the attachment  
 177 of molecular dopants and could result in carrier concentrations  
 178 of ungated graphene around 10<sup>11</sup> cm<sup>-2</sup> as compared to as-  
 179 grown monolayer graphene with substrate-induced doping as  
 180 high as  $n \approx 10^{13}$  cm<sup>-2</sup>. We note that both of the components of  
 181 aqua regia, nitric acid and hydrochloric acid, are potent p-  
 182 doping agents of graphene.<sup>39,40</sup> Please see more details of the  
 183 fabrication (Supporting Information S3). Finally, we trans-  
 184 ferred an h-BN layer on top of the ribbon as a dielectric layer  
 185 and fabricated a top gate to control carrier density of the  
 186 graphene ribbon device.

## 187 ■ RESULTS AND DISCUSSION

188 In this work, in addition to the self-assembled graphene  
 189 ribbons (type A) which have been described earlier, for  
 190 comparison, we fabricated devices from a different type of  
 191 graphene ribbons (type B), which were etched by RIE from  
 192 large-area epitaxial graphene (Figure 4b). Edges of these  
 193 graphene ribbons become irregular due to the resolution of the  
 194 electron-beam lithographic techniques. Moreover, their edges  
 195 could be doped by chemicals from subsequent fabrication

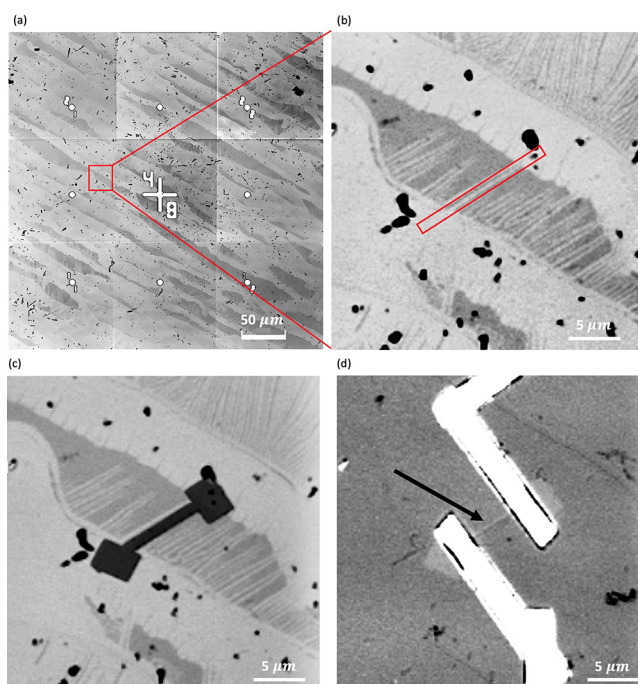


**Figure 3.** (a) A 360  $\mu\text{m} \times 360 \mu\text{m}$  CLSM image after we evaporated a gold protection layer ( $\approx 20$  nm thick) on top of the whole substrate. The gray (dark) regions correspond to graphene ribbons (IFL/SiC). The bright white regions indicate Pt alignment marks. (b) A magnification of the selected area shown in (a). The chosen graphene ribbon was labeled by the red, unfilled rectangle. (c) A CLSM image after we evaporated a thicker gold pattern on the ribbon. A second gold pattern (a dark gray region) instead of PMMA was deposited to protect the graphene ribbon. The brightness of the gold covered area is darker than that of graphene because the reflective energy of an Au pattern is smaller than that of graphene. (d) A CLSM image after the Pt contacts are fabricated. The gold pattern was etched by dilute aqua regia, and the single graphene ribbon indicated by the black arrow is visible at the center. The bright white regions correspond to Pt contacts.

because the gold pattern cannot cover the edges of a graphene  
 196 ribbon. In contrast, for type A devices that were made from  
 197 self-assembled graphene ribbon, the Au pattern was wider than  
 198 the ribbon and protected the surface and the edges of graphene  
 199 ribbons, guaranteeing cleaner and more uniform edges (Figure  
 200 4a). The overlaying Au layers on top of graphene ribbons in  
 201 both cases were completely removed by dilute aqua regia.  
 202

We performed two-terminal resistance measurements on  
 203 two types of graphene ribbon devices at low temperatures.  
 204 Unless otherwise stated, the measurement temperature was 0.1  
 205 K. In order to study possible MR peaks caused by boundary  
 206 scattering<sup>14–16</sup> in the graphene ribbons, we must first account  
 207 for the reproducible conductance fluctuations clearly seen in  
 208 Supporting Information S4. They are present as a function of  
 209 magnetic field  $B$  and are caused by the fact that the graphene  
 210 devices are small and comparable to the dephasing length.<sup>41</sup>  
 211 The resistance results are averaged over a range of  $B = 0.05$  T  
 212 so that the averaged data clearly show the changes in resistance  
 213 of the sample without the obscurity due to universal  
 214 conductance fluctuations<sup>41</sup> (Supporting Information S4).  
 215

Figure 5 shows the measurement results of a device made  
 216 from a self-assembled graphene ribbon whose length and width  
 217 are 2.5  $\mu\text{m}$  and 300 nm, respectively. Its Dirac point was  
 218 observed when top gate was swept to  $V_g = -12.5$  V, confirming  
 219

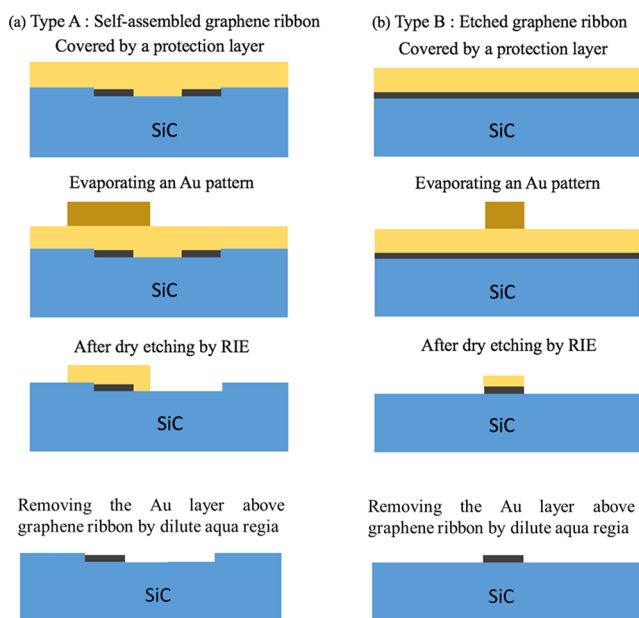


**Figure 4.** Schematic diagrams showing the difference between two types of graphene ribbon device fabrication processes. The first Au layer (yellow regions) protected graphene (black regions) from polymer contamination in the subsequent process. A second Au layer (dark yellow regions) was patterned to cover selected area for a graphene ribbon. The blue regions correspond to SiC. (a) The self-assembled ribbon (type A) width is determined by the epitaxial growth process. Consequently, a larger Au pattern is produced to cover the edges of the ribbon to protect it from chemicals. (b) For a sample with an etched ribbon (type B), a homogeneous graphene monolayer region was selected. The width of the etched ribbon was determined by the second Au pattern in the RIE process.

220 that it is an n-type graphene ribbon (Figure 5a). With weak  
 221 backscattering from smooth edges, the MR ratio  $[R(B) - R(B$   
 222  $= 0)]/R(B = 0)$  is  $\approx 3\%$  for  $V_g = -9$  V and  $V_g = -10$  V (Figure  
 223 5b). The anomalous MR behaviors of a type A ribbon are  
 224 dominated by boundary scattering.<sup>14–16</sup> Our experimental  
 225 results are consistent with diffusive boundary scattering from  
 226 clean graphene edges in the quasi-ballistic regime as described  
 227 as follows. The properties of magnetotransport rely on the size  
 228 of the cyclotron radius. At low magnetic fields, a carrier  
 229 cyclotron orbit is much larger than the widths of samples,  $r_c \gg$   
 230  $W$ , and carriers were scattered diffusively on the edge (the solid  
 231 curve in the inset of Figure 5c). The MR curve shows evidence  
 232 for weak localization (WL) due to intervalley scattering<sup>41</sup> from  
 233 the sharp edges, and WL was quenched with increasing  
 234 temperature as shown in Figure 5d. As magnetic field increases,  
 235 the cyclotron radius by the Lorentz force becomes similar to  
 236 the ribbon width,  $r_c \approx W$  (the dashed curve in the inset of  
 237 Figure 5c), leading to increasing resistance due to increasing  
 238 collisions from the edges of samples and the probability of  
 239 backscattering. At higher magnetic fields, the cyclotron radius  
 240 is smaller than the width,  $r_c < W$ . In this case, an orbit that  
 241 travels along the edges is formed, and the probability of  
 242 backscattering is decreased (the dotted curve in the inset of  
 243 Figure 5c). The resistance is again diminished with increasing  
 244 magnetic field. In Figure 5c, two side resistance peaks are  
 245 observed where the  $B_{\max}$  corresponds to the local maximal  
 246 value of MR when the cyclotron radius is close to the width.  
 247 Similar results are obtained in an ungated 190 nm wide self-  
 248 assembled graphene ribbon (Supporting Information S5). This

relationship between the cyclotron radius and the width can be  
 249 described by the proportionality constant  $\alpha = W/r_c$ . For the  
 250 boundary scattering model for graphene,  $\alpha$  is equal to  $0.9 \pm$   
 251  $0.1$ .<sup>15,16</sup> In a 2D system, the cyclotron radius can be written as  
 252  $r_c(B, n) = \left(\frac{\hbar}{eB}\right)\sqrt{\pi n}$ , where  $e$  is the elementary charge,  $n$  is the  
 253 carrier density, and  $\hbar$  is the reduced Planck constant. Thus,  
 254  $B_{\max}$  can be well described by the equation  
 255

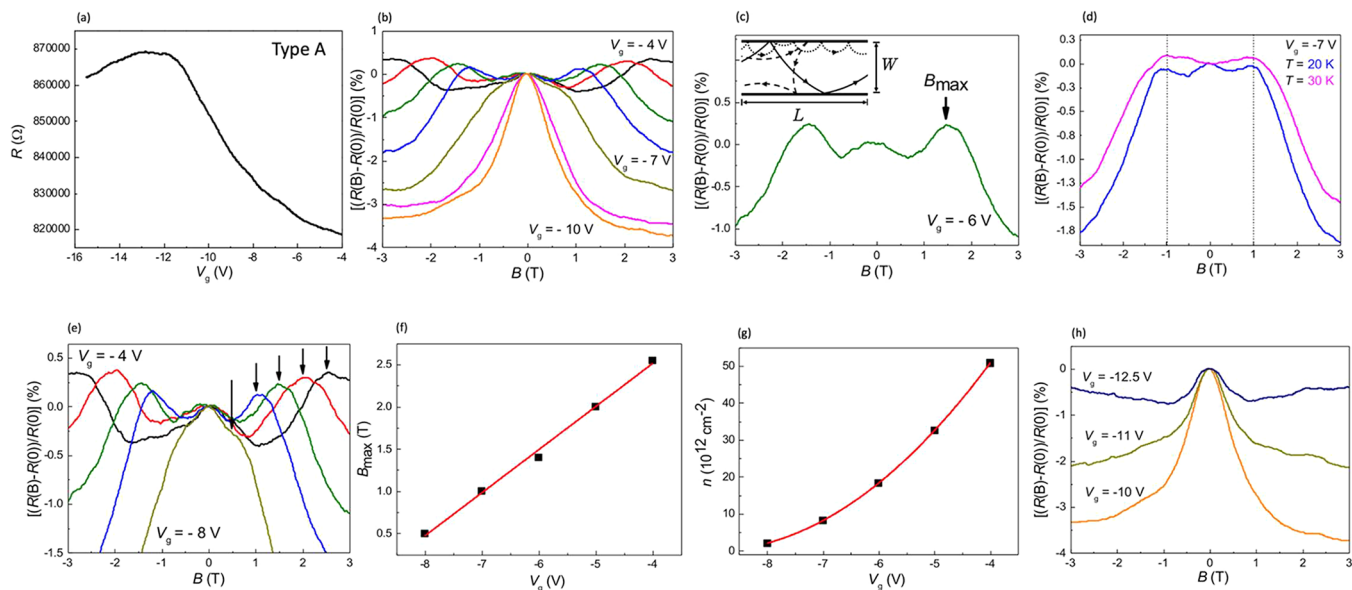
$$B_{\max} = \alpha \frac{\hbar \sqrt{\pi n}}{e W} \quad (1)$$

Figure 5d shows that the  $B_{\max}$  is independent of temperature  
 257 and is only affected by the carrier density as described by eq 1.  
 258 To further study  $B_{\max}$ , we measure the MR at different top gate  
 259 voltages. Figure 5e shows the MR ratio as a function of  $B$  at  
 260 gate voltages  $V_g = -4, -5, -6, -7,$  and  $-8$  V. The  $B_{\max}$  is  
 261 shifted with varying gate voltages. We find that the  $B_{\max}$  has a  
 262 linear dependence on gate voltage (Figure 5f). According to eq  
 263 1,  $B_{\max} \propto \sqrt{n}$ ; therefore, it is deduced that  $n \propto V_g^2$  which will  
 264 be explained in the following. In the Drude model, the carrier  
 265 density  $n_D$  is proportional to  $V_g$ , which is expressed as  $n_D =$   
 266  $\frac{C_{\text{ox}}}{e}(V_g - V_D)$ , where  $C_{\text{ox}}$  is the geometric capacitance of the  
 267 gate oxide and  $V_D$  is the voltage corresponding to the Dirac  
 268 point.<sup>42</sup> However, if the thickness of the insulator of the top  
 269 gate is small (for this sample, the h-BN layer is  $\approx 26$  nm thick),  
 270 the quantum capacitances from interfaces of the top gate  
 271 should be considered.<sup>43,44</sup> Under these conditions,  $n(V_g)$  can  
 272 be described by the equation

$$n + \frac{C_{s1} + C_{s2}}{e^2} \varepsilon_F = \frac{1}{1 + C_{\gamma 2}/C_{c2}} \frac{C_{\text{ox}}}{e} (V_g - V_D) \quad (2)$$

Here,  $\varepsilon_F$  is the Fermi level of the graphene ribbon and is  
 274 expressed as  $\varepsilon_F = \hbar v \sqrt{\pi n}$ , where  $v$ , the Fermi velocity, is equal  
 275 to  $1.15 \times 10^6$  m/s. The quantum capacitance of interfaces is  
 276 described by the capacitive items. The interface between the  
 277 IFL and graphene is labeled by  $i = 1$ , and the interface (or  
 278 dopants from fabrication) between h-BN and graphene is  
 279 labeled by  $i = 2$ . The geometrical capacitance is described by  
 280  $C_{ci} = \varepsilon_i/d_i$ , where  $\varepsilon_i$  is the dielectric constant and  $d_i = 0.3$  nm is  
 281 the distance between the graphene and its adjacent  
 282 neighboring layers.<sup>43</sup> The quantum capacitance is expressed  
 283 as  $C_{\gamma i} = \gamma_i e^2$ , where  $\gamma_i$  is a parameter which corresponds to the  
 284 chemical potential. Consequently, we can obtain the total  
 285

capacitance parameter as  $C_{si} = \left(\frac{1}{C_{ci}} + \frac{1}{C_{\gamma i}}\right)^{-1}$ . If the thickness  
 286 of dielectric layer is more than a few hundred nanometers,  $C_{\text{ox}}$   
 287 is dominant. The quantum capacitances are ignored, and eq 2  
 288 becomes  $n_D = (C_{\text{ox}}/e)(V_g - V_D)$ . By solving eq 2, we deduce  
 289 that  $n \propto V_g^2$  (Supporting Information S6). This result is the  
 290 same as that from boundary scattering and proves that  
 291 boundary scattering model fits this sample well. Putting  $B_{\max}$ ,  
 292  $W$ , and  $V_g$  in eq 1, we can obtain the carrier density as a  
 293 function of gate voltage  $V_g$  as shown in Figure 5g. As we have  
 294 two-terminal devices, at present we are not able to eliminate  
 295 the contact resistance which may actually dominate the  
 296 measured two-terminal resistance. Moreover, we are not able  
 297 to measure the Hall effect and are only able to measure the  
 298 carrier density by  $B_{\max}$  by using eq 1. We can, however,  
 299 estimate the mobility in the self-assembled graphene ribbon by  
 300 the carrier density by referring to an earlier work done on  
 301 continuous graphene.<sup>29</sup> In this case, the low-temperature 302



**Figure 5.** MR behavior for the self-assembled graphene ribbon whose width is 300 nm. (a) Resistance as a function of gate bias voltage. The maximal resistance, the Dirac point, is observed at  $V_g = -12.5$  V. (b) MR ratio as a function of  $B$  measured at gate voltages  $V_g = -4, -5, -6, -7, -8, -9,$  and  $-10$  V (from top to bottom). Anomalous MR behaviors are observed. (c) MR ratio as a function of  $B$  at  $V_g = -6$  V, and the WL effect is dominant below 1 T. With increasing magnetic field, above 1 T, the MR transport is dominated by boundary scattering. The  $B_{\max}$  is at 1.5 T. Inset: a schematic diagram showing trajectories of carriers in devices for  $r_c \gg W$  (the solid curve),  $r_c \geq W$  (the dashed curve), and  $r_c < W$  (the dotted curve). (d) Normalized resistance as a function of  $B$  measured at  $V_g = -7$  V and  $T = 20$  and  $30$  K. The WL effect is suppressed at a higher temperature, but the  $B_{\max}$  as shown by the dashed lines is still observed apparently. (e) MR curves as a function of  $B$  measured at varying gate voltages  $V_g = -4, -5, -6, -7,$  and  $-8$  V (from top to bottom). Positions of the  $B_{\max}$  as indicated by black arrows are dependent on the gate voltage. For clarity, only  $B_{\max}$  for positive  $B$  are labeled. (f)  $B_{\max}$  as a function of gate voltage, as inferred from (e) ( $B_{\max} \propto V_g$ ). There is a good linear fit to the data (red line). (g) The carrier densities as a function of gate voltage is obtained by putting the  $B_{\max}$ ,  $W$ , and gate voltage in eq 1. There is a good quadratic fit to the data (red curve). Boundary scattering happened at  $n \geq 10^{12} \text{ cm}^{-2}$ . (h) MR ratio as a function of  $B$  measured at gate voltages  $V_g = -10, -11,$  and  $-12.5$  V. At  $V_g = -12.5$  V, the carrier density is low; when  $B > 1$  T and  $B < -1$  T, positive magnetoresistance due to classical diffusive scattering<sup>16</sup> is observed.

303 mobility of our self-assembled graphene ribbon is estimated to  
304 be between 3000 and 5000  $\text{cm}^2/(\text{V s})$ .

305 We note that experimental evidence for diffusive boundary  
306 scattering is observed when the carrier density is higher than  
307  $10^{12} \text{ cm}^{-2}$ . As shown in Figure 5h, at  $V_g = -10$  V,  $V_g = -11$  V,  
308 and  $V_g = -12.5$  V, we were not able to observe  $B_{\max}$  consistent  
309 with the fact that  $B_{\max}$  approaches zero at  $V_g = -9$  V as  
310 suggested by extrapolating the linear fit shown in Figure 5f.  
311 Near the Dirac point at  $V_g = -12.5$  V, when  $B > 1$  T and  $B <$   
312  $1$  T positive magnetoresistance due to classical diffusive  
313 scattering<sup>16</sup> is observed.

314 Figure 6 shows the results of a type B graphene ribbon  
315 whose length and width are 5  $\mu\text{m}$  and 200 nm, respectively.  
316 We were not able to observe the Dirac point and  $B_{\max}$ ;  
317 therefore, we cannot estimate the carrier density as well as the  
318 mobility of etched graphene ribbons (Figure 6a). Strong  
319 negative MR behavior is observed (Figure 6b) and is  
320 independent of gate bias voltage (Figure 6c). The MR ratio  
321 is  $\approx 13\%$ , larger than that reported in Figure 5b. We speculate  
322 that this phenomenon is not from the dopants or defects on  
323 surfaces of samples. Based on the VRH model,<sup>45</sup> the MR  
324 behavior has a transition from WL to strong negative MR with  
325 decreasing the carrier density, if the graphene surface contains  
326 defects and chemical dopants that may create a high random  
327 barrier for electronic transport. However, at  $V_g = -14$  V, the  
328 MR does not show a strong  $T$  dependence (Figure 6d). When  
329 the measurement temperature is varied by a factor of 20, the  
330 MR only changes by around 4% (Figure 6e), suggesting that  
331 VRH is not the dominant mechanism. In our type B graphene

332 ribbons, the MR behaviors are independent of gate voltage  
333 (and hence carrier density), suggesting that the graphene  
334 surface remains sufficiently clean during our fabrication and  
335 that the graphene is also sufficiently uniform so that there is  
336 little disorder. We speculate that the negative MR is due to the  
337 dopants or defects on the edge of graphene ribbons. Irregular  
338 edges of ribbons can cause a higher probability of back-  
339 scattering. When magnetic field is provided, paths of carriers  
340 become shorter due to the cyclotron radius and decreases the  
341 probability of backscattering. Consequently, the resistance is  
342 decreased, and it causes strong negative MR behavior. This  
343 behavior is still observed in wider samples, as the one shown in  
344 Figure 6f, whose width is 570 nm (length = 5  $\mu\text{m}$ ). Its MR  
345 ratio is smaller, 9%, possibly due to the edge effect being  
346 suppressed with increasing the sample width. The absence of  
347 the MR side peak due to diffusive boundary scattering in these  
348 two devices suggests that the edge smoothness of etched  
349 graphene ribbons is lower than that of epitaxially grown  
350 graphene ribbon device. Since both type A and type B ribbons  
351 are fabricated on the same SiC substrate, the interface of the  
352 ribbons to the SiC substrate should not play an important role  
353 in their vastly different transport properties. It is known that  
354 the edge effect become dominant with decreasing the width. In  
355 the seminal work by Masubushi et al. on boundary scattering in  
356 graphene,<sup>15</sup> the widths of their samples are around 1  $\mu\text{m}$ . In  
357 this case, the edge effect is relatively weak, and it may not be  
358 necessary to consider the causality between smooth edges and  
359 edge scattering. In contrast, with narrower graphene width, the  
360 rough edges may result in the strong backscattering and affects

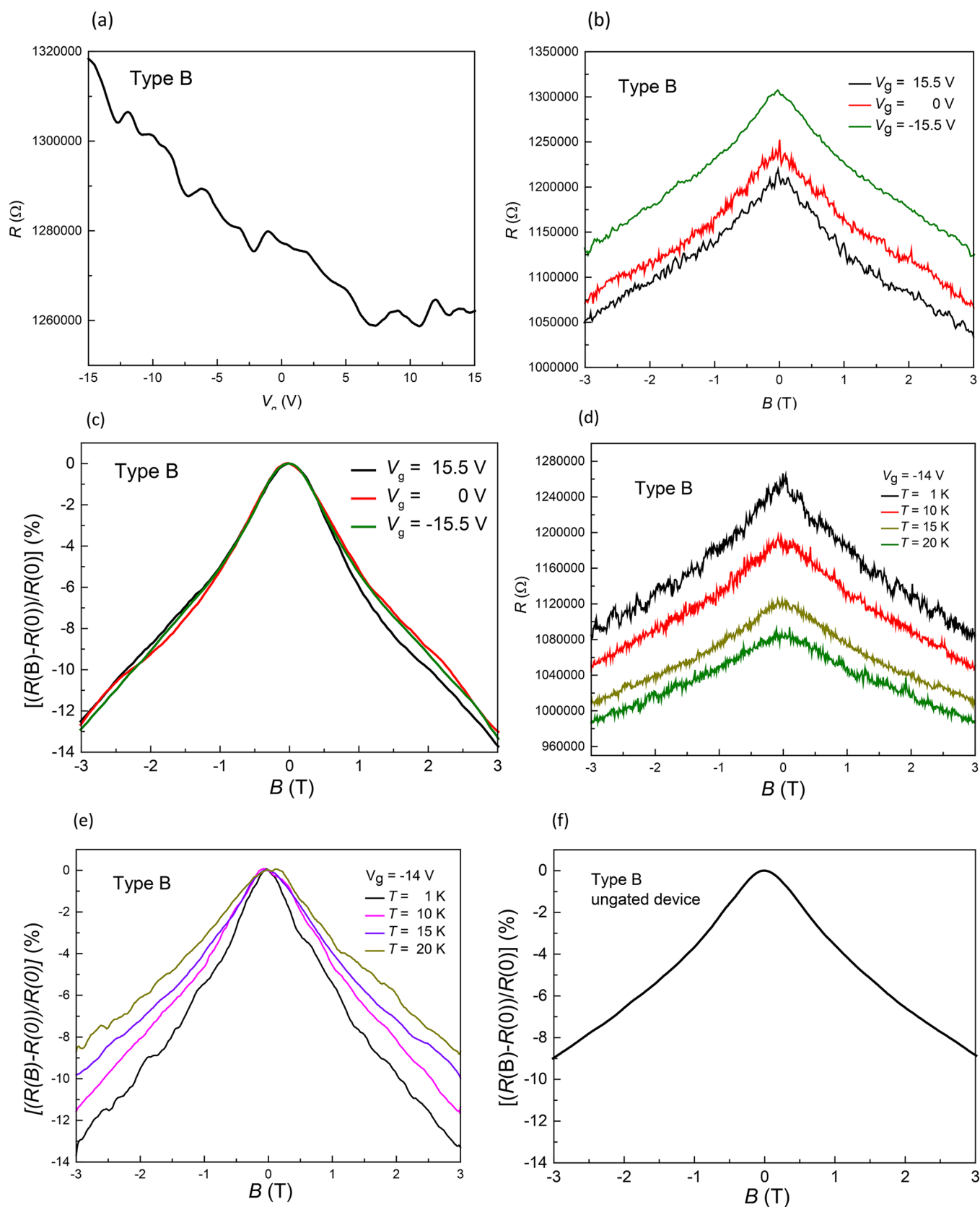


**Figure 6.** MR behavior for etched ribbons (type B). (a) Resistance as a function of gate voltage. (b) Resistance as a function of magnetic field at different gate voltages. (c) The width of the etched ribbon is 200 nm. Averaged MR ratio as a function of  $B$  measured at gate bias voltage =  $-15.5$ ,  $0$ , and  $15.5$  V. Strong negative MR is observed and independent of gate bias voltage. The MR ratio is roughly 13%. (d) Magnetoresistance at  $V_g = -14$  V at different temperatures. (e) MR at  $V_g = -14$  V at different temperatures. (f) Averaged normalized resistance as a function of  $B$  for another etched ribbon whose width is larger, 570 nm. In this wider sample, the strong negative MR still exists, and the MR ratio is 9%, which is smaller than that observed in the narrower, etched graphene ribbon shown in (c).

the edge scattering. We note that in ref 16 graphene edges as atomically sharp defects dominate the elastic and inelastic intervalley scattering, and the inelastic scattering mechanism is electron–electron intervalley scattering in the ballistic regime. Both diffusive boundary scattering as characterized by  $B_{\max}$  and intervalley scatterings (WL) were observed simultaneously in their graphene sample, consistent with our experimental results obtained on self-assembled graphene ribbons. Therefore, the graphene edge properties should play an important role in the transport in graphene ribbons. The vastly different edge preparation between our self-assembled and etched graphene ribbons appears to be the key factor in determining the MR properties of our ribbon devices.

We would like to point out that the length to width ratio ( $2.5 \mu\text{m}/300 \text{ nm}$ ) of device type A is different from that of device type B ( $5 \mu\text{m}/200 \text{ nm}$ ). Therefore, the resistivity, rather than the resistance, is perhaps the suitable physical quantity to estimate the carrier densities of the graphene ribbon devices. We note that for at  $V_g = -9 \text{ V}$  the resistivity of device type A is about  $100 \text{ k}\Omega$ . On the other hand, at  $V_g = 0 \text{ V}$ , the resistivity of device type B is about  $50 \text{ k}\Omega$ . If the resistivity can be used to estimate the carrier concentration, the carrier density of device type B at  $V_g = 0$  is higher than that of device type A at  $V_g = -9 \text{ V}$ . Moreover, we believe that the applied gate voltage is a more suitable physical quantity to estimate the carrier density of the graphene ribbon. For device type B, the Dirac point may well be lower than  $-15.5 \text{ V}$  since we do not see a local minimum around  $V_g = -15.5 \text{ V}$ . Even if the Dirac point is at  $-15.5 \text{ V}$ , at  $V_g = 0$ , the voltage difference between the applied gate voltage and the Dirac point is  $15.5 \text{ V}$ . In contrast, for device type A, at  $V_g = -9 \text{ V}$ , the voltage difference between the applied gate voltage and the Dirac point ( $V_D = -12.5 \text{ V}$ ) is  $3.5 \text{ V}$ . Assuming that the carrier density is proportional to  $(V_g - V_D)^2$ , the carrier density at  $V_g = 0 \text{ V}$  for device B is at least  $16 (=4^2)$  times higher than that for device type A at  $V_g = -9 \text{ V}$ . The fact that no MR side peak is observed at device type B at  $V_g = 0$  cannot be due to the low carrier density (device type A at  $V_g = -9 \text{ V}$ ). Therefore, we can exclude the possibilities of low density in device type B for not observing the MR side peak. The most probable reason for this is the edge roughness in device type B due to etching.

## CONCLUSIONS

We studied the edge effect in graphene ribbons through magnetotransport measurements. We found that self-assembled graphene ribbons on SiC have been prepared by the high-temperature sublimation technique similar to the method for growing large-area monolayer graphene on a SiC substrate. Compared to SEM and Raman spectra studies, the CLSM scans the sample rapidly in only 10 min and covers a large area in ambient conditions. The spatial resolution of the CLSM image is high,  $\approx 150 \text{ nm}$ ,<sup>13</sup> and it is an efficient approach to choose suitable graphene ribbons for device fabrication even when a gold protection layer ( $\approx 20 \text{ nm}$ ) is deposited on top of the ribbon. Such a thin gold layer can protect both the top surface and edges of the graphene ribbon from contamination by PMMA and other residues. Selecting a single high-quality graphene ribbon with smooth edges allows us to observe a MR side peak which is consistent with the commensurability effect between the ribbon width and cyclotron radius. By using a high-quality, thin h-BN layer as a dielectric, we are able to apply a top gate voltage in order to study the evolution of the anomalous MR peak as a function of

carrier density. In contrast, an etched graphene ribbon, which is also protected by a gold layer during the fabrication process, only shows large negative MR effect due to suppression of backscattering near rough graphene edges with increasing magnetic field. Our approach based on efficient CLSM studies and a metallic protection layer paves the way for preparing high-quality self-assembled graphene ribbons for practical device applications in terahertz sensors, interconnects, and plasmonic devices, all of which can be fabricated on a wafer-scale SiC substrate.

## EXPERIMENTAL METHODS

**Confocal Laser Scanning Microscopy (CLSM).** In this work, CLSM images of multilayer graphene, graphene, graphene ribbons, and IFL/SiC were obtained by using an Olympus LEXT OLS4100 system fitted with  $\times 5$ ,  $\times 10$ ,  $\times 20$ ,  $\times 50$ , and  $\times 100$  objective lenses (numerical apertures: 0.15, 0.30, 0.60, 0.95, and 0.95, respectively) and with up to  $\times 8$  further optical zoom.<sup>13</sup> This allows us to use the CLSM to image an area with field of view ranging from  $2560 \mu\text{m} \times 2560$  to  $16 \mu\text{m} \times 16 \mu\text{m}$  in a single step. Many such images can be combined by an automatic stitching process. The CLSM system employs a 405 nm wavelength violet semiconductor laser, which is scanned in the X–Y directions by an electromagnetic microelectromechanical systems scanner and a high-precision mirror galvanometer, and a photomultiplier to capture the reflected light and generate images up to  $4096 \times 4096$  pixels with horizontal spatial resolution of  $150 \text{ nm}$ .<sup>13</sup> As a noninvasive technique, CLSM does not modify the graphene/SiC interface.

**Atomic Force Microscopy (AFM).** We performed AFM studies of graphene, IFL/SiC, and graphene ribbons in tapping-mode in air using a Bruker Dimension FastScan scanning probe microscope. In this mode, the probe oscillates at its fundamental resonance ( $f_0$ ) and a feedback loop tracks the surface of the sample by adjusting the Z-piezo height to maintain a constant amplitude of the cantilever oscillation.<sup>13</sup>

**Raman Spectroscopy.** The Raman spectra and mapping of IFL/SiC, graphene, graphene ribbons, and multilayer graphene were obtained under ambient conditions with  $633 \text{ nm}$  excitation (Renishaw InVia), which is focused to an  $\sim 0.8 \mu\text{m}$  spot on the samples through a  $\times 100$  objective (0.85 NA). Raman maps were performed by raster scanning the laser with a step size of  $100 \text{ nm}$  and collecting the spectra with an exposure time of  $1 \text{ s}$  for each point,  $1800 \text{ mm}^{-1}$  grating, and high confocality ( $20 \mu\text{m}$  slit opening). Raman maps of the G and 2D peaks area, intensity, width, and shift were generated from fitting the data.<sup>13</sup>

**Low-Temperature Electrical Measurements.** The low-temperature experiments of graphene ribbon devices were performed in an Oxford Triton 200 cryo-free dilution refrigerator. Two-terminal resistance measurements were performed using standard ac lock-in techniques. Unless otherwise stated, the measurement temperature was  $0.1 \text{ K}$ .

## ASSOCIATED CONTENT

### Supporting Information

The Supporting Information is available free of charge at <https://pubs.acs.org/doi/10.1021/acsaelm.9b00696>.

AFM and CLSM imaging for identifying monolayer graphene ribbons, crystal orientation of self-assembled graphene ribbon arrays, fabrication of graphene ribbon by e-beam lithography reactive ion etching, data averaging, evidence for diffusive boundary scattering as indicated by the observation of  $B_{\max}$  in an ungated self-assembled graphene ribbon, and the relation between the carrier density and the top gate voltage when the dielectric layer is thin (PDF)

## 486 ■ AUTHOR INFORMATION

## 487 Corresponding Authors

488 **Randolph E. Elmquist** – National Institute of Standards  
489 and Technology (NIST), Gaithersburg, Maryland;

490 Email: [randolph.elmquist@nist.gov](mailto:randolph.elmquist@nist.gov)

491 **Chi-Te Liang** – National Taiwan University, Taipei,  
492 Taiwan;  [orcid.org/0000-0003-4435-5949](https://orcid.org/0000-0003-4435-5949);

493 Email: [ctliang@phys.ntu.edu.tw](mailto:ctliang@phys.ntu.edu.tw)

## 494 Other Authors

495 **Bi-Yi Wu** – National Institute of Standards and  
496 Technology (NIST), Gaithersburg, Maryland, and  
497 National Taiwan University, Taipei, Taiwan

498 **Yanfei Yang** – National Institute of Standards and  
499 Technology (NIST), Gaithersburg, Maryland

500 **Albert F. Rigosi** – National Institute of Standards and  
501 Technology (NIST), Gaithersburg, Maryland

502 **Jiuning Hu** – National Institute of Standards and  
503 Technology (NIST), Gaithersburg, Maryland

504 **Hsin-Yen Lee** – National Institute of Standards and  
505 Technology (NIST), Gaithersburg, Maryland

506 **Guangjun Cheng** – National Institute of Standards and  
507 Technology (NIST), Gaithersburg, Maryland

508 **Vishal Panchal** – National Institute of Standards and  
509 Technology (NIST), Gaithersburg, Maryland, and  
510 National Physical Laboratory, Teddington, U.K.

511 **Mattias Kruskopf** – National Institute of Standards and  
512 Technology (NIST), Gaithersburg, Maryland, and  
513 University of Maryland, College Park, Maryland

514 **Hanbyul Jin** – National Institute of Standards and  
515 Technology (NIST), Gaithersburg, Maryland, and  
516 University of Maryland, College Park, Maryland

517 **Kenji Watanabe** – National Institute for Materials  
518 Science, Tsukuba, Japan

519 **Takashi Taniguchi** – National Institute for Materials  
520 Science, Tsukuba, Japan

521 **David B. Newell** – National Institute of Standards and  
522 Technology (NIST), Gaithersburg, Maryland

523 Complete contact information is available at:

524 <https://pubs.acs.org/10.1021/acsaelm.9b00696>

## 525 Author Contributions

526 B.-Y.W. and Y.Y. contributed equally to this work. B.-Y.W.  
527 performed sample fabrication, measurements, data analyses,  
528 and managed the project direction. Y.Y. prepared self-  
529 assembled graphene ribbons on SiC, provided the fabrication  
530 methods, assisted with sample fabrication, and managed the  
531 project direction. A.F.R. assisted with sample characterization  
532 and measurements. J.H. and H.Y.L. assisted with sample  
533 fabrication. G.C., V.P., M.K., and H.J. assisted with sample  
534 characterization. K.W. and T.T. provided h-BN materials for  
535 sample fabrication. R.E.E. and C.T.L. contributed overall  
536 project ideas. All authors have approved the final manuscript.

## 537 Notes

538 The authors declare no competing financial interest.

## 539 ■ ACKNOWLEDGMENTS

540 The work of B.-Y.W. at NIST was made possible by  
541 arrangement with Prof. Chi-Te Liang of National Taiwan

University. B.-Y.W. and C.T.L. acknowledge support from the 542  
Ministry of Science and Technology (MOST), Taiwan (Grants 543  
MOST 105-2119-M-002-048-MY3, MOST 105-2112-M-002- 544  
005-MY3, MOST 108-2622-8-002-016, and MOST108-2119- 545  
M-002-025-MY3) and National Taiwan University (Grants 546  
107L892101 and 108L892101). A.F.R. thanks the National 547  
Research Council for the opportunity. K.W. and T.T. 548  
acknowledge support from the Elemental Strategy Initiative 549  
conducted by the MEXT, Japan, and the CREST 550  
(JPMJCR15F3), JST. The authors thank J. Hagmann and S. 551  
Zhang for their assistance in internal review. 552

## 553 ■ REFERENCES

- 554 (1) Novoselov, K. S.; Geim, A. K.; Morozov, S. V.; Jiang, D.; 555  
Katsnelson, M. I.; Grigorieva, I. V.; Dubonos, S. V.; Firsov, A. A. Two- 556  
dimensional gas of massless Dirac fermions in graphene. *Nature* **2005**, 557  
438, 197–200.
- 558 (2) Zhang, Y. B.; Tan, Y. W.; Stormer, H. L.; Kim, P. Experimental 559  
observation of the quantum Hall effect and Berry's phase in graphene. 560  
*Nature* **2005**, 438, 201–204.
- 561 (3) Du, X.; Skachko, I.; Duerr, F.; Luican, A.; Andrei, E. Y. 562  
Fractional quantum Hall effect and insulating phase of Dirac electrons 563  
in graphene. *Nature* **2009**, 462, 192–195.
- 564 (4) Bolotin, K. I.; Ghahari, F.; Shulman, M. D.; Stormer, H. L.; Kim, 565  
P. Observation of the fractional quantum Hall effect in graphene. 566  
*Nature* **2009**, 462, 196–199.
- 567 (5) Young, A. F.; Kim, P. Quantum interference and Klein tunnelling 568  
in graphene heterojunctions. *Nat. Phys.* **2009**, 5, 222–226.
- 569 (6) Moors, K.; Contino, A.; van de Put, M. L.; Vandenbergh, W. 570  
G.; Fischetti, M. V.; Magnus, W.; Soree, B. Theoretical study of 571  
scattering in graphene ribbons in the presence of structural and 572  
atomistic edge roughness. *Phys. Rev. Materials* **2019**, 3, 024001.
- 573 (7) Sols, F.; Guinea, F.; Castro Neto, A. H. Coulomb blockade in 574  
graphene nanoribbons. *Phys. Rev. Lett.* **2007**, 99, 166803.
- 575 (8) Bai, J. W.; Cheng, R.; Xiu, F. X.; Liao, L.; Wang, M. S.; Shailos, 576  
A.; Wang, K. L.; Huang, Y.; Duan, X. F. Very large magnetoresistance 577  
in graphene nanoribbons. *Nat. Nanotechnol.* **2010**, 5, 655–659.
- 578 (9) Misawa, T.; Okanaga, T.; Mohamad, A.; Sakai, T.; Awano, Y. 579  
Line width dependence of transport properties in graphene nano- 580  
ribbon interconnects with real space edge roughness determined by 581  
Monte Carlo method. *Jpn. J. Appl. Phys.* **2015**, 54, 05EB01.
- 582 (10) Yang, W. Y.; Wu, B. Y.; Shih, C. J.; Lo, S. T.; Lee, H. Y.; Chen, 583  
T. M.; Chang, Y. H.; Chen, Y. F.; Liang, C. T. Unveiling conducting 584  
pathways embedded in strongly disordered graphene. *Semicond. Sci.* 585  
*Technol.* **2016**, 31, 115001.
- 586 (11) Liu, C. I.; Wu, B. Y.; Chuang, C. S.; Lee, Y. C.; Ho, Y. J.; Yang, 587  
Y. F.; Elmquist, R. E.; Lo, S. T.; Liang, C. T. Variable range hopping 588  
and nonlinear transport in monolayer epitaxial graphene grown on 589  
SiC. *Semicond. Sci. Technol.* **2016**, 31, 105008.
- 590 (12) Berger, C.; Song, Z. M.; Li, T. B.; Li, X. B.; Ogbazghi, A. Y.; 591  
Feng, R.; Dai, Z. T.; Marchenkov, A. N.; Conrad, E. H.; First, P. N.; 592  
de Heer, W. A. Ultrathin epitaxial graphite: 2D electron gas properties 593  
and a route toward graphene-based nanoelectronics. *J. Phys. Chem. B* 594  
**2004**, 108, 19912–19916.
- 595 (13) Panchal, V.; Yang, Y. F.; Cheng, G. J.; Hu, J. N.; Kruskopf, M.; 596  
Liu, C. I.; Rigosi, A. F.; Melios, C.; Walker, A. R. H.; Newell, D. B.; 597  
Kazakova, O.; Elmquist, R. E. Confocal laser scanning microscopy for 598  
rapid optical characterization of graphene. *Commun. Phys.* **2018**, 1, 83.
- 599 (14) Thornton, T. J.; Roukes, M. L.; Scherer, A.; Vandegaag, B. P. 600  
Boundary scattering in quantum wires. *Phys. Rev. Lett.* **1989**, 63, 601  
2128–2131.
- 602 (15) Masubuchi, S.; Iguchi, K.; Yamaguchi, T.; Onuki, M.; Arai, M.; 603  
Watanabe, K.; Taniguchi, T.; Machida, T. Boundary scattering in 604  
ballistic graphene. *Phys. Rev. Lett.* **2012**, 109, 036601.
- 605 (16) Huang, J.; Guo, L. W.; Li, Z. L.; Chen, L. L.; Lin, J. J.; Jia, Y. P.; 606  
Lu, W.; Guo, Y.; Chen, X. L. Anisotropic quantum transport in a 607  
network of vertically aligned graphene sheets. *J. Phys.: Condens. Matter* 608  
**2014**, 26, 345301.

- (17) Behnam, A.; Lyons, A. S.; Bae, M. H.; Chow, E. K.; Islam, S.; Neumann, C. M.; Pop, E. Transport in nanoribbon interconnects obtained from graphene grown by chemical vapor deposition. *Nano Lett.* **2012**, *12*, 4424–4430.
- (18) Murali, R.; Brenner, K.; Yang, Y. X.; Beck, T.; Meindl, J. D. Resistivity of graphene nanoribbon interconnects. *IEEE Electron Device Lett.* **2009**, *30*, 611–613.
- (19) Bao, Q. L.; Loh, K. P. Graphene photonics, plasmonics, and broadband optoelectronic devices. *ACS Nano* **2012**, *6*, 3677–3694.
- (20) Vasic, B.; Isic, G.; Gajic, R. Localized surface plasmon resonances in graphene ribbon arrays for sensing of dielectric environment at infrared frequencies. *J. Appl. Phys.* **2013**, *113*, 013110.
- (21) Farquhar, A. K.; Supur, M.; Smith, S. R.; Dyck, C.; McCreery, R. L. Hybrid graphene ribbon/carbon electrodes for high-performance energy storage. *Adv. Energy Mater.* **2018**, *8*, 1802439.
- (22) Nikitin, A. Y.; Guinea, F.; Garcia-Vidal, F. J.; Martin-Moreno, L. Edge and waveguide terahertz surface plasmon modes in graphene microribbons. *Phys. Rev. B: Condens. Matter Mater. Phys.* **2011**, *84*, 161407.
- (23) Low, T.; Avouris, P. Graphene plasmonics for terahertz to mid-infrared applications. *ACS Nano* **2014**, *8*, 1086–1101.
- (24) Sprinkle, M.; Ruan, M.; Hu, Y.; Hankinson, J.; Rubio-Roy, M.; Zhang, B.; Wu, X.; Berger, C.; de Heer, W. A. Scalable templated growth of graphene nanoribbons on SiC. *Nat. Nanotechnol.* **2010**, *5*, 727–731.
- (25) Baringhaus, J.; Ruan, M.; Edler, F.; Tejada, A.; Sicot, M.; Taleb-Ibrahimi, A.; Li, A.-P.; Jiang, Z.; Conrad, E. H.; Berger, C.; Tegenkamp, C.; de Heer, W. A. Exceptional ballistic transport in epitaxial graphene nanoribbons. *Nature* **2014**, *506*, 349–354.
- (26) Baringhaus, J.; Settnes, M.; Aprojanz, J.; Power, S. R.; Jauho, A.-P.; Tegenkamp, C. Electron interference in ballistic graphene nanoconstrictions. *Phys. Rev. Lett.* **2016**, *116*, 186602.
- (27) Baringhaus, J.; Aprojanz, J.; Wiegand, J.; Laube, D.; Halbauer, M.; Hübner, J.; Oestreich, M.; Tegenkamp, C. Growth and characterization of sidewall graphene nanoribbons. *Appl. Phys. Lett.* **2015**, *106*, 043109.
- (28) Aprojanz, J.; Bampoulis, P.; Zakharov, A. A.; Zandvliet, H. J. W.; Tegenkamp, C. Nanoscale imaging of electric pathways in epitaxial graphene nanoribbons. *Nano Res.* **2019**, *12*, 1697–1702.
- (29) Yang, Y.; Cheng, G. J.; Mende, P.; Calizo, I. G.; Feenstra, R. M.; Chuang, C.; Liu, C. W.; Liu, C. I.; Jones, G. R.; Walker, A. R. H.; Elmquist, R. E. Epitaxial graphene homogeneity and quantum Hall effect in millimeter-scale devices. *Carbon* **2017**, *115*, 229–236.
- (30) Tromp, R. M.; Hannon, J. B. Thermodynamics and kinetics of graphene growth on SiC(0001). *Phys. Rev. Lett.* **2009**, *102*, 106104.
- (31) Ohta, T.; Bartelt, N. C.; Nie, S.; Thurmer, K.; Kellogg, G. L. Role of carbon surface diffusion on the growth of epitaxial graphene on SiC. *Phys. Rev. B: Condens. Matter Mater. Phys.* **2010**, *81*, 121411.
- (32) Kruskopf, M.; Elmquist, R. E. Epitaxial graphene for quantum resistance metrology. *Metrologia* **2018**, *55*, R27–R36.
- (33) Kruskopf, M.; Pakdehi, D. M.; Pierz, K.; Wundrack, S.; Stosch, R.; Dziomba, T.; Gotz, M.; Baringhaus, J.; Aprojanz, J.; Tegenkamp, C.; Lidzba, J.; Seyller, T.; Hohls, F.; Ahlers, F. J.; Schumacher, H. W. Comeback of epitaxial graphene for electronics: large-area growth of bilayer-free graphene on SiC. *2D Mater.* **2016**, *3*, 041002.
- (34) Nair, M. N.; Palacio, I.; Celis, A.; Zobelli, A.; Gloter, A.; Kubsky, S.; Turmaud, J. P.; Conrad, M.; Berger, C.; de Heer, W.; Conrad, E. H. Band gap opening induced by the structural periodicity in epitaxial graphene buffer layer. *Nano Lett.* **2017**, *17*, 2681–2689.
- (35) Hill, H. M.; Rigosi, A. F.; Chowdhury, S.; Yang, Y.; Nguyen, N. V.; Tavazza, F.; Elmquist, R. E.; Newell, D. B.; Walker, A. R. H. Probing the dielectric response of the interfacial buffer layer in epitaxial graphene via optical spectroscopy. *Phys. Rev. B: Condens. Matter Mater. Phys.* **2017**, *96*, 195437.
- (36) Nevius, M. S.; Wang, F.; Mathieu, C.; Barrett, N.; Sala, A.; Menteş, T. O.; Locatelli, A.; Conrad, E. H. The bottom-up growth of edge specific graphene nanoribbons. *Nano Lett.* **2014**, *14*, 6080–6086.
- (37) Yang, Y.; Huang, L. I.; Fukuyama, Y.; Liu, F. H.; Real, M. A.; Barbara, P.; Liang, C. T.; Newell, D. B.; Elmquist, R. E. Low carrier density epitaxial graphene devices on SiC. *Small* **2015**, *11*, 90–95.
- (38) Williams, K. R.; Gupta, K. M.; Wasilik, M. Etch rates for micromachining processing—part II. *J. Microelectromech. Syst.* **2003**, *12*, 761–778.
- (39) Wehling, T. O.; Novoselov, K. S.; Morozov, S. V.; Vdovin, E. E.; Katsnelson, M. I.; Geim, A. K.; Lichtenstein, A. I. Molecular doping of graphene. *Nano Lett.* **2008**, *8*, 173–177.
- (40) Bae, S.; Kim, H.; Lee, Y.; Xu, X.; Park, J.-S.; Zheng, Y.; Balakrishnan, J.; Lei, T.; Kim, H. R.; Song, Y. I.; Kim, Y.-J.; Kim, K. S.; Özyilmaz, B.; Ahn, J.-H.; Hong, B. H.; Iijima, S. Roll-to-roll production of 30-in. graphene films for transparent electrodes. *Nat. Nanotechnol.* **2010**, *5*, 574–578.
- (41) Tikhonenko, F. V.; Kozikov, A. A.; Savchenko, A. K.; Gorbachev, R. V. Transition between electron localization and antilocalization in graphene. *Phys. Rev. Lett.* **2009**, *103*, 226801.
- (42) Ashcroft, N.; Mermin, N. *Solid State Physics*; Saunders College: 1976.
- (43) Takase, K.; Tanabe, S.; Sasaki, S.; Hibino, H.; Muraki, K. Impact of graphene quantum capacitance on transport spectroscopy. *Phys. Rev. B: Condens. Matter Mater. Phys.* **2012**, *86*, 165435.
- (44) Hu, J.; Rigosi, A. F.; Kruskopf, M.; Yang, Y.; Wu, B. Y.; Tian, J. F.; Panna, A. R.; Lee, H. Y.; Payagala, S. U.; Jones, G. R.; Kraft, M. E.; Jarrett, D. G.; Watanabe, K.; Taniguchi, T.; Elmquist, R. E.; Newell, D. B. Towards epitaxial graphene p–n junctions as electrically programmable quantum resistance standards. *Sci. Rep.* **2018**, *8*, 15018.
- (45) Hong, X.; Cheng, S. H.; Herding, C.; Zhu, J. Colossal negative magnetoresistance in dilute fluorinated graphene. *Phys. Rev. B: Condens. Matter Mater. Phys.* **2011**, *83*, 085410.

## Supporting Information

### A self-assembled graphene ribbon device on SiC

Bi-Yi Wu<sup>1, 2, †</sup>, Yanfei Yang<sup>1, †</sup>, Albert F. Rigosi<sup>1</sup>, Jiuning Hu<sup>1</sup>, Hsin-Yen Lee<sup>1</sup>, Guangjun Cheng<sup>1</sup>, Vishal Panchal<sup>1, 3</sup>, Mattias Kruskopf<sup>1, 4</sup>, Hanbyul Jin<sup>1, 4</sup>, Kenji Watanabe<sup>5</sup>, Takashi Taniguchi<sup>5</sup>, David B. Newell<sup>1</sup>, Randolph E. Elmquist<sup>1, \*</sup>, and Chi-Te Liang<sup>2, \*</sup>  
<sup>1</sup>Physical Measurement Laboratory, National Institute of Standards and Technology (NIST), Gaithersburg, MD 20899, USA  
<sup>2</sup>Graduate Institute of Applied Physics, National Taiwan University, Taipei 10617, Taiwan  
<sup>3</sup>National Physical Laboratory, Hampton Road, Teddington, TW11 0LW, UK  
<sup>4</sup>Joint Quantum Institute (JQI), University of Maryland, College Park, MD 20742, USA  
<sup>5</sup>National Institute for Materials Science, 1-1 Namiki, Tsukuba 305-0044, Japan

<sup>†</sup>These authors contributed equally to this work

\*randolph.elmquist@nist.gov and ctliang@phys.ntu.edu.tw

#### S1 AFM and CLSM imaging for identifying monolayer graphene ribbons

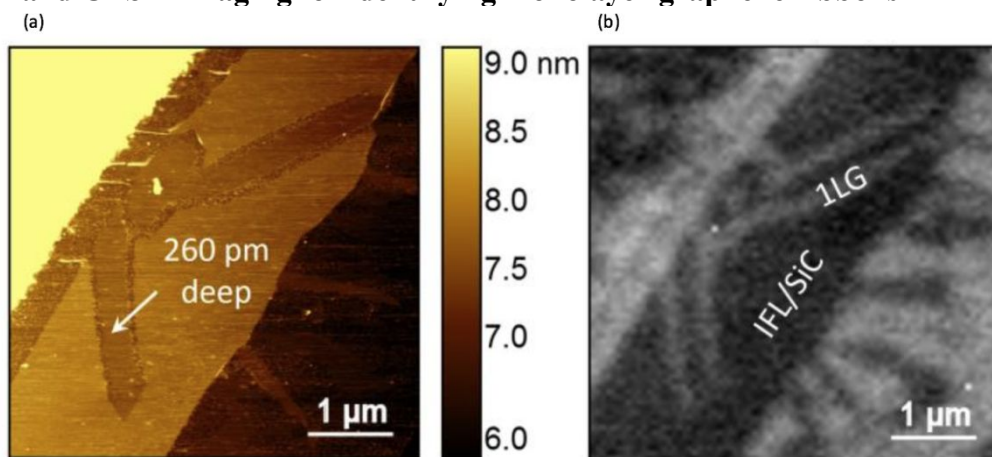


Figure S1. (a) An AFM image of self-assembled graphene ribbons. The different brightness of color corresponds to the different terraces. The thickness of the sublimation area which is pointed out in the middle terrace by the white arrow is 260 nm. (b) A CLSM image of graphene ribbons in the same region as (a). The grey regions correspond to graphene ribbons or large-area graphene (1LG). The dark regions indicate the interfacial layer (IFL) or SiC substrate. Graphene ribbons are found on the edge of each straight SiC sublimation area.

We can confirm the mechanism of growing graphene ribbons by the AFM image as shown in figure S1 (a). In the AFM image, three terraces are in the different brightness of colors. In the middle terrace, the SiC sublimation area which is formed from the edge of the terrace is observed. The thickness of the sublimation area indicated by the white arrow in figure S1 (a) is 260 nm and blurring graphene ribbons on the edge of the sublimation area is observed. We can compare the AFM image with the CLSM image as shown in figure S1 (b), and two graphene ribbons on the edge of each straight sublimation area are observed. It proves that the mechanism of the growing graphene ribbons is determined by the surface diffusion of Si atoms.

## S2 Crystal orientation of self-assembled graphene ribbon arrays

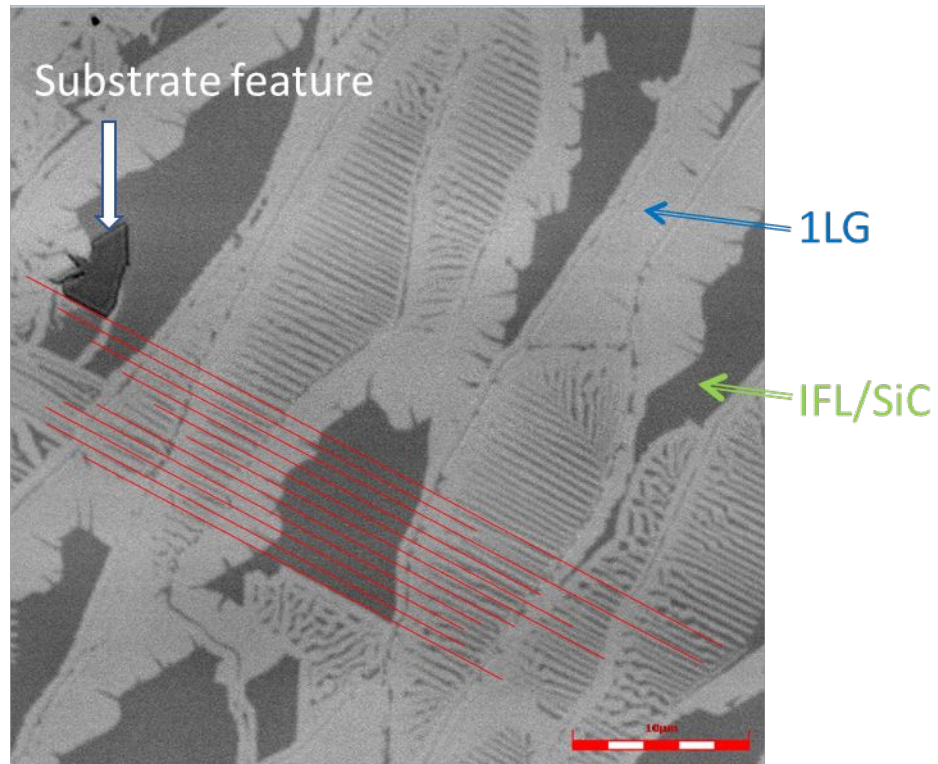


Figure S2. A CLSM image of graphene ribbon arrays. The edges in natural graphene ribbon arrays form primarily along the SiC $\langle 11\bar{2}0 \rangle$  direction as indicated by the red lines. The scale is 10  $\mu\text{m}$ . The green and blue arrows indicated the IFL/SiC and one-layer graphene (1LG) regions, respectively.

### S3 Fabrication of graphene ribbon by e-beam lithography reactive ion etching

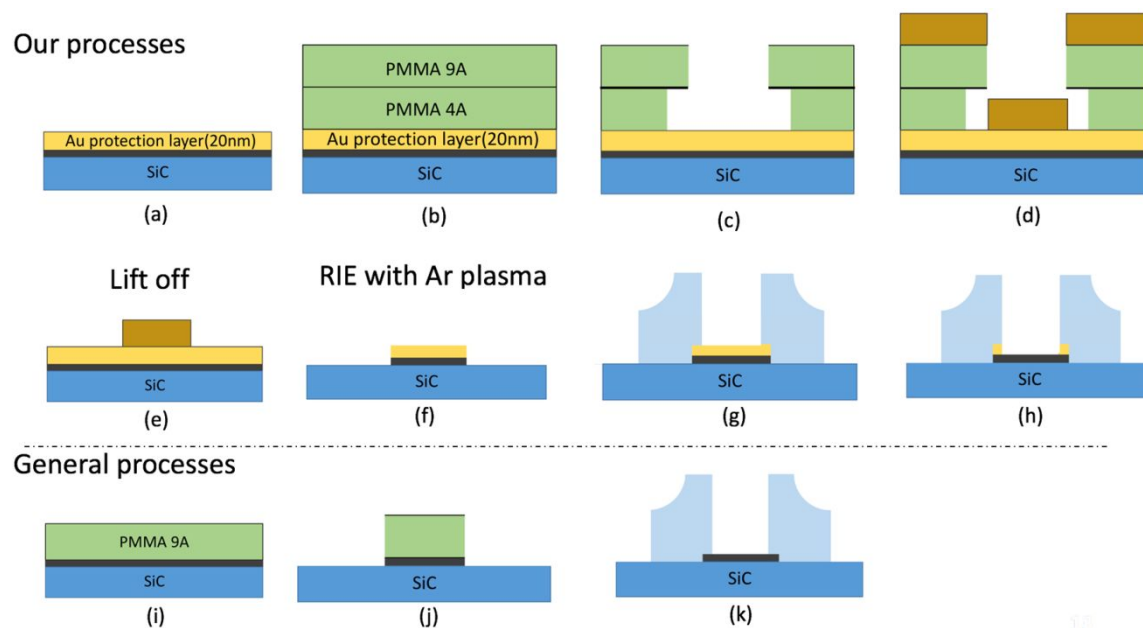


Figure S3. Schematic diagrams showing the contamination-free processes in our fabrication. The blue regions correspond to the SiC substrate. The black regions correspond to graphene on SiC. The green regions indicate the resist, PMMA, for electron-beam lithography. (a) A 20-nm-thick Au layer (the yellow region) is evaporated to protect graphene. (b) Spin-coating of bilayer electron-beam resists, PMMA. (c) To expose the pattern with electron-beam lithographic techniques. (d) A 35-nm-thick Au layer (the dark yellow region) is fabricated to make gold patterns. (e) Lift-off in acetone. (f) Graphene is dry etched with Ar plasma by RIE. The Au patterns determine the shapes of graphene. (g) Pt is used as electrical contacts to graphene which correspond to the bright blue regions. (h) Put the devices in dilute aqua regia (DAR) and DAR only etched the Au layers. Graphene is visible at the center. (i) In general processes, PMMA touches directly graphene and doped it. (j) Use PMMA patterns to determine shapes of devices when graphene is dry etched with O<sub>2</sub> plasma by RIE. (k) When electrical contacts, which are the bright blue regions, are fabricated, PMMA touches directly the graphene again.

We use a contamination-free processes in our fabrication. To protect graphene from contamination of PMMA residues, first we evaporate a 20-nm-thick Au layer on surfaces (figure 2 (a)). Next, Au patterns (figure 2 (f)) were adopted instead of PMMA patterns (figure 2 (j)) since metal layer on the top and graphene are etched by Ar plasma with RIE. Au patterns determine the shapes of devices. In addition, we adopt Pt to make contacts with general processes (figure 2 (g)). Finally, devices are put in dilute aqua regia (DAR). DAR only etches the Au layer at the center and Pt contacts, which have an anti-erosion effect of DAR, remain on the device (figure 2 (h)). Residues of resists, PMMA, disappear when the protective metal layer is removed by DAR. With these processes, surfaces of graphene are protected from chemical and keep the graphene surface remarkably clean.

## S4 Data averaging

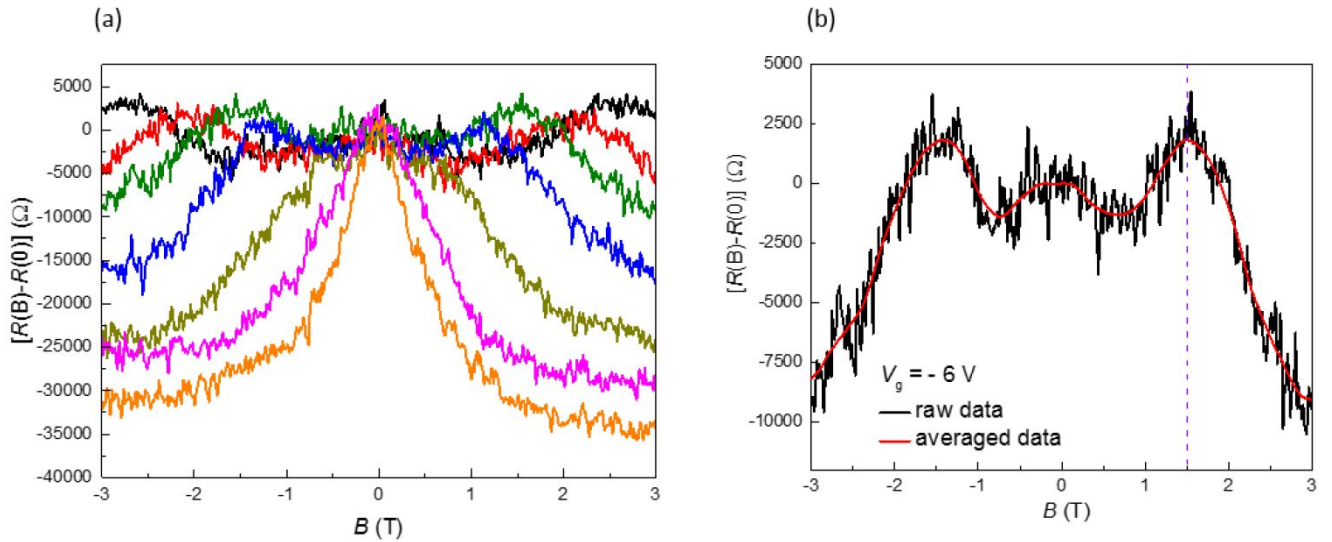


Figure S4. (a)  $R(B)-R(B=0)$  as function of  $B$  at  $V_g = -4$  V,  $-5$  V,  $-6$  V,  $-7$  V,  $-8$  V,  $-9$  V and  $-10$  V (from top to bottom). Universal conductance fluctuations (UCFs) exit at different gate voltages (b) The black curve corresponds to  $R(B)-R(0)$  as function of  $B$  at  $V_g = -6$  V. Red dashed curve shows that the averaged data. We can label the  $B_{max}$  as the purple dashed line in the MR curve which is with stronger UCFs. After averaging the resistance in each region, the weak localization become clear as shown in red curve.

Universal conductance fluctuations (UCFs) exist in mesoscopic devices, because the interference of carriers waves travels along the graphene device. In figure S3 (a), the resistance fluctuations are observed at different gate voltages. Though fluctuations were too strong to distinguish the weak localization from the MR structure, we could also determine the  $B_{max}$  apparently by the maximal resistance (figure 3 (b)). To suppress the effect of UCFs, the resistance results are averaged over a range of  $B = 0.05$  T. The red curve shown in figure 3 (b) is the averaged result and the weak localization effect becomes clearer at low magnetic fields<sup>1</sup>.

**S5 Evidence for diffusive boundary scattering as indicated by the observation of  $B_{\max}$  in an ungated self-assembled graphene ribbon.**

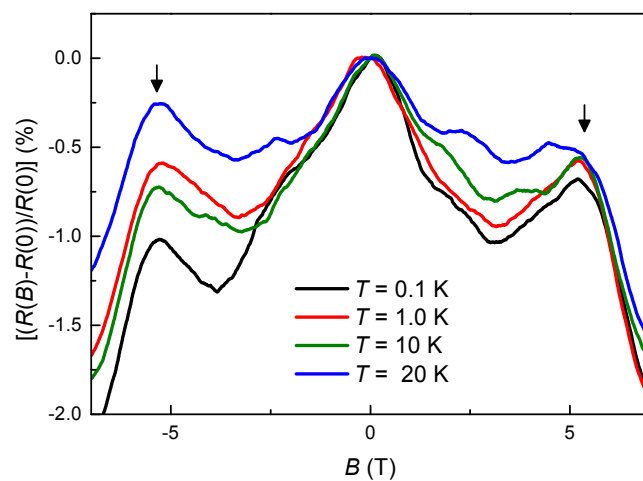


Figure S5 MR as a function of magnetic field at various temperatures. The data was taken on an ungated 190-nm-wide self-assembled graphene ribbon. The arrows indicate  $B_{\max}$  due to diffusive boundary scattering.

**S6 The relation between the carrier density and the top gate voltage when the dielectric layer is thin**

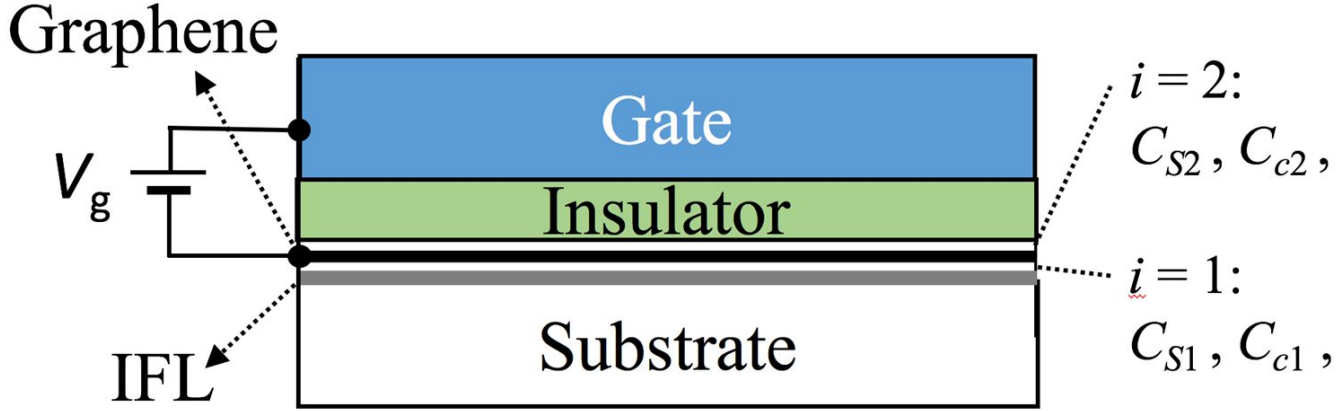


Figure S5. Schematic diagram showing a top-gated graphene device. The grey and black region indicate the IFL and graphene, respectively. The interface between the IFL and graphene is labelled by  $i=1$ , and the interface between graphene and the insulator (dielectric) layer is labelled by  $i=2$ .

Figure S6 shows a top-gated graphene device. If the thickness of the insulator of the top gate is small,  $n(V_g)$  can be described by Eq. (2)

$$n + \frac{C_{s1} + C_{s2}}{e^2} \varepsilon_F = \frac{1}{1 + C_{r2}/C_{c2}} \frac{C_{ox}}{e} (V_g - V_D).$$

where  $\varepsilon_F = \hbar v \sqrt{\pi n}$ . We can suppose that  $A = \frac{C_{s1} + C_{s2}}{e^2} \hbar v \sqrt{\pi}$ ,  $B = \frac{1}{1 + C_{r2}/C_{c2}} \frac{C_{ox}}{e}$  and  $V_{eff} =$

$(V_g - V_D)$ . Eq. (2) can be re-written as

$$n + A\sqrt{n} = BV_{eff}. \quad (3)$$

We can solve equation (3) and obtain that

$$n(V_{eff}) = BV_{eff} + \frac{1}{2}A^2 \pm \sqrt{\frac{1}{4}A^4 + BA^2V_{eff}}$$

The third term can be expanded by the binomial theorem as the following equation

$$\sqrt{\frac{1}{4}A^4 + BA^2V_{eff}} = \left( \frac{1}{2}A^2 + BV_{eff} - \frac{B^2}{A^2}V_{eff}^2 + 2\frac{B^3}{A^4}V_{eff}^3 + \dots \right).$$

Then, we know that carrier density is equal to 0 when  $V_{eff} = 0$ , and the constant term in this equation should be equal to 0. Consequently, Eq. (3) is re-written as

$$\begin{aligned} n(V_{eff}) &= BV_{eff} + \frac{1}{2}A^2 - \sqrt{\frac{1}{4}A^4 + BA^2V_{eff}} \\ &= BV_{eff} + \frac{1}{2}A^2 - \left( \frac{1}{2}A^2 + BV_{eff} - \frac{B^2}{A^2}V_{eff}^2 + 2\frac{B^3}{A^4}V_{eff}^3 + \dots \right) \end{aligned}$$

$$= \frac{B^2}{A^2} V_{\text{eff}}^2 - 2 \frac{B^3}{A^4} V_{\text{eff}}^3 + \dots \quad (4)$$

We can estimate that  $A \approx 10^7$  and  $B \approx 10^{11}$  with parameters<sup>2</sup> listed as below: (1)  $\epsilon_{BN} = 3.9\epsilon_0$ ,  $\epsilon_1 = 9.7\epsilon_0$ , and  $\epsilon_2 = 3\epsilon_0$ , where  $\epsilon_0$  is the vacuum permittivity (2)  $\gamma_1 = 1.2 \times 10^{14} \text{eV}^{-1} \text{cm}^{-2}$  and  $\gamma_2 = 1.5 \times 10^4 \text{eV}^{-1} \text{cm}^{-2}$  (3)  $d_{\text{ox}} = 45 \text{ nm}$ ,  $d_1 = d_2 = 0.3 \text{ nm}$  and we obtain that  $\frac{B^2}{A^2} \gg \frac{B^3}{A^4}$ .

Thus, Eq. (4) is approximated by the following equation

$$n(V_{\text{eff}}) = \frac{B^2}{A^2} V_{\text{eff}}^2. \quad (5)$$

## References

- (1) Tikhonenko, F. V.; Kozikov, A. A.; Savchenko, A. K.; Gorbachev, R. V. Transition between Electron Localization and Antilocalization in Graphene. *Phys. Rev. Lett.* **2009**, *103*, 226801.
- (2) Hu, J.; Rigosi, A. F.; Kruskopf, M.; Yang, Y.; Wu, B. Y.; Tian, J. F.; Panna, A. R.; Lee, H. Y.; Payagala, S. U.; Jones, G. R.; Kraft, M. E.; Jarrett, D. G.; Watanabe, K.; Taniguchi, T.; Elmquist, R. E.; Newell, D. B. Towards epitaxial graphene p-n junctions as electrically programmable quantum resistance standards. *Sci. Rep.* **2018**, *8*, 15018.